Journal of Applied Pharmaceutical Science 2025. Article in Press
Available online at http://www.japsonline.com
DOI: 10.7324/JAPS.2026.256031
ISSN 2231-3354

Discovery of pyrazole–pyrazoline derivatives as VEGFR-2 kinase inhibitors: *In silico* approach

Deepali M. Wanode*, Kumud P. Bhendarkar, Pramod B. Khedekar
Department of Pharmaceutical Sciences, Rashtrasant Tukadoji Maharaj Nagpur University, Nagpur, India.

ARTICLE HISTORY
Received on: 04/05/2025
Accepted on: 30/06/2025
Available Online: XX

Key words:
Pyrazole, pyrazoline, molecular docking, VEGFR-2, ADMET.

ABSTRACT

Angiogenesis, the formation of new blood vessels, plays an important role in tumor growth and metastasis. Vascular endothelial growth factor receptor-2 (VEGFR-2) is a key regulator of this process and a crucial target for anti-angiogenic cancer therapies. In this work, a series of pyrazole–pyrazoline derivatives were designed by incorporating various heterocyclic moieties, such as thiazole, benzothiazole, pyridine, furan, thiophene, and pyrrole, to improve VEGFR-2 inhibition. Using an *in silico* approach, molecular docking studies with AutoDock Vina revealed strong binding interactions, particularly hydrophobic and hydrogen bonding, with amino acid residues of the VEGFR-2 protein. The compounds were tested for pharmacokinetic properties and drug-likeness using SwissADME, and their absorption, distribution, metabolism, excretion, and toxicity profiles were predicted through the pkCSM tool. Among the tested compounds, C-64 emerged as the most promising lead candidate, showing optimum binding affinity, compliance with Lipinski's and Veber's rules, and no predicted hepatotoxicity, cardiotoxicity, or mutagenicity. Moreover, C-64 displayed a high LD_{50} value, suggesting low toxicity, and the lowest total clearance, indicating prolonged retention. It also aligned well with key physicochemical parameters in the bioavailability radar and was positioned in the white region of the BOILED-Egg model, suggesting efficient gastrointestinal absorption. These findings position C-64 as a promising candidate for further optimization and preclinical development in cancer therapy.

1. INTRODUCTION

Angiogenesis is a vital physiological process involving the formation of new blood vessels from pre-existing vasculature [1]. It plays a central role in various biological events, including inflammation and wound healing. However, in the context of pathological angiogenesis, such as in cancer, newly formed blood vessels infiltrate tumor masses, supplying essential oxygen and nutrients that support tumor growth and facilitate metastasis [2]. Consequently, targeting angiogenesis has emerged as a promising therapeutic approach to inhibit tumor progression, potentially offering fewer side effects compared to conventional chemotherapies [3]. Among the angiogenic factors, vascular endothelial growth factor (VEGF)plays a crucial role in angiogenesis [4]. VEGF activates VEGF receptor (VEGFR) tyrosine kinases (VEGFR-1, VEGFR-2, and VEGFR-3), leading to endothelial cell proliferation and neovascularization [5]. Notably, VEGFR-2 is recognized as the key mediator of VEGF-driven angiogenic signaling [6]. Accordingly, inhibition of VEGFR-2 signaling has been recognized as a significant therapeutic strategy for the development of new agents targeting angiogenesis-dependent human cancers. VEGFR-2 kinase inhibitors are broadly categorized into two primary classes based on their binding modes. Type I inhibitors are ATP (adenosine triphosphate)-competitive and bind to the active conformation of the kinase, occupying the ATP-binding site, specifically the region normally engaged by the adenine moiety of ATP. In contrast, type II inhibitors stabilize the kinase in its inactive DFG (Aspartate–Phenylalanine–Glycine)-out conformation, allowing them to extend into an adjacent allosteric hydrophobic pocket near the ATP-binding site, thereby offering enhanced selectivity and prolonged target engagement [7].

---

*Corresponding Author
Deepali M. Wanode, Department of Pharmaceutical Sciences, Rashtrasant Tukadoji Maharaj Nagpur University, Nagpur, India.
E-mail: dipwanode @ gmail.com

The pyrazole scaffold has received significant attention due to its wide spectrum of pharmacological activities and has emerged as a valuable pharmacophore in the design and development of potent anticancer agents [8]. Notably, various studies have reported the strong inhibitory potential of pyrazole-based derivatives against VEGFR-2 kinase, highlighting their promise as targeted anti-angiogenic therapeutics [9,10]. Furthermore, several studies have demonstrated that pyrazole derivatives substituted at the 1-, 3-, and 4-positions reveal increased antiproliferative effect [11–13] as well as potent inhibition of VEGFR-2 kinase [1,14]. Pyrazole compounds linked with other heterocyclic systems have exhibited promising cytotoxic activity. The incorporation of additional aromatic or heteroaromatic rings such as benzene, benzothiazole [1], thiazole [15,16], pyridine [17,18], furan [19], thiophene [20], and pyrrole [14,19] has been shown to significantly increase VEGFR-2 inhibitory potency. Moreover, hybrid compounds combining pyrazole with pyrazoline have demonstrated strong cytotoxic and VEGFR-2 inhibitory activities, with efficacy observed in the micromolar to nanomolar range [14].

In light of the aforementioned findings, the current study was undertaken to design a series of 1,3,4-trisubstituted pyrazole derivatives, incorporating a pyrazoline moiety at the 4-position and various heterocyclic substituents such as thiazole, benzothiazole, pyridine, furan, thiophene, and pyrrole at the first and fourth positions. The objective was to determine potent VEGFR-2 kinase inhibitors with reduced toxicity and favorable interaction profiles. To this end, molecular docking studies were carried out to elucidate the binding modes of the designed compounds within the active site of the VEGFR-2 kinase enzyme. Additionally, absorption, distribution, metabolism, excretion, and toxicity (ADMET) profiling and drug-likeness assessment were conducted to further assess the pharmacokinetic behavior, stability, and therapeutic potential of the compounds.

2. MATERIALS AND METHODS

2.1. Molecular docking

The structures of ligands were initially sketched using ChemDraw Professional 15.0 and saved in Structure data file (SDF) (chemical file format used to store molecular structures and associated data) format. These 2D structures were then converted into 3D SDF format, followed by file format conversion to PDBQT using Open Babel. Hydrogen atoms were subsequently added using AutoDock Tools to prepare the ligands for molecular docking, and the finalized ligand files were saved in PDBQT format. The crystal structure of protein VEGFR-2 kinase was retrieved from the Protein Data Bank (PDB ID: 4ASD) and tested for structural quality using the PROCHECK program. The potential binding pockets were identified using the CASTp3.0 server, which enabled the precise mapping of active site cavities. These predicted binding regions were then utilized to define the most suitable ligand-binding site within the target protein. Subsequently, the protein was prepared by deleting non-essential entities, including crystallographic water molecules and extraneous ligands, to ensure a pristine receptor environment. Protein preparation for molecular docking was executed using AutoDock Tools, with the binding site meticulously delineated based on the coordinates of the co-crystallized ligand. A configuration file (config.txt) was generated to specify the docking parameters, including the grid box dimensions and the coordinates of its center (x, y, z), thereby defining the 3D search space within the active site of the target protein. The exhaustiveness parameter was set to optimize the thoroughness of the conformational search.

To establish the reliability and precision of the docking protocol, validation was done by redocking the co-crystallized ligand. This redocking procedure served to validate the computational methodology and ensure the robustness of the docking parameters. The optimized and validated protocol was subsequently applied to investigate ligand–receptor interactions of the designed compounds. These docking simulations aimed to elucidate the binding conformations, predict interaction profiles within the VEGFR-2 active site, and provide mechanistic insights into the observed anticancer activity of the compounds.

Docking simulations were performed using AutoDock Vina via the command line interface. The working directory was navigated to include all necessary input files: AutoDock Vina executable, prepared protein, ligand PDBQT files, and the configuration file. Upon execution, AutoDock Vina produced output files detailing the predicted binding poses and their corresponding binding affinities. The ligand design strategy is illustrated in Figure 1, and the structural details of the designed compounds are summarized in Table 1.

2.2. Drug likeness and synthetic accessibility evaluation

The drug-likeness and synthetic accessibility of the designed compounds were evaluated using the SwissADME web tool. Critical physicochemical parameters such as molecular weight, number of hydrogen bond donors and acceptors, and lipophilicity (log P) were determined, all of which were in accordance with Lipinski's rule of five,

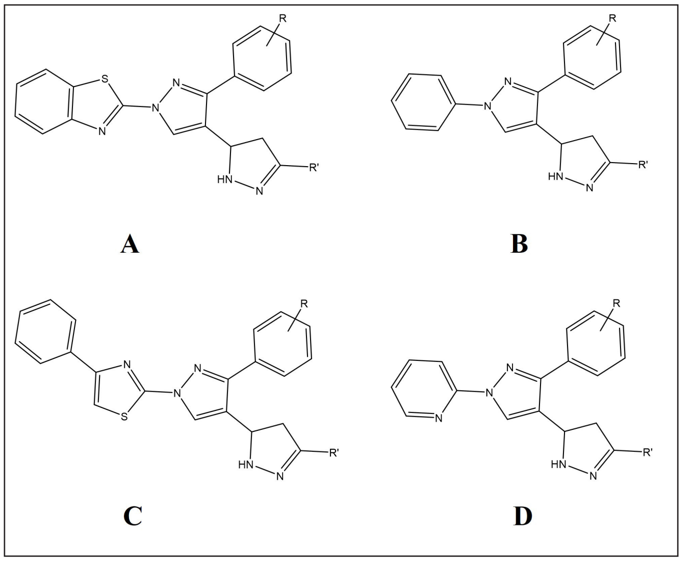

Figure 1. Designed pyrazole–pyrazoline derivatives—A, B, C, and D series.

Table 1. Designed pyrazole–pyrazoline derivatives.

Compound code	R	R’	Compound Code	R	R’
A/B/C/D/-1	4-CH_3	2-furyl	A/B/C/D/-41	4-CH_3	2-pyrrolyl
A/B/C/D/-2	4-OCH_3	2-furyl	A/B/C/D/-42	4-OCH_3	2-pyrrolyl
A/B/C/D/-3	4-Br	2-furyl	A/B/C/D/-43	4-Br	2-pyrrolyl
A/B/C/D/-4	2-OH	2-furyl	A/B/C/D/-44	2-OH	2-pyrrolyl
A/B/C/D/-5	3-NO_2	2-furyl	A/B/C/D/-45	3-NO_2	2-pyrrolyl
A/B/C/D/-6	4-NO_2	2-furyl	A/B/C/D/-46	4-NO_2	2-pyrrolyl
A/B/C/D/-7	4-F	2-furyl	A/B/C/D/-47	4-F	2-pyrrolyl
A/B/C/D/-8	4-Cl	2-furyl	A/B/C/D/-48	4-Cl	2-pyrrolyl
A/B/C/D/-9	4-OH	2-furyl	A/B/C/D/-49	4-OH	2-pyrrolyl
A/B/C/D/-10	2-NH_2	2-furyl	A/B/C/D/-50	2-NH_2	2-pyrrolyl
A/B/C/D/-11	3-NH_2	2-furyl	A/B/C/D/-51	3-NH_2	2-pyrrolyl
A/B/C/D/-12	2,4-di OH	2-furyl	A/B/C/D/-52	2,4-di OH	2-pyrrolyl
A/B/C/D/-13	2-Br, 4-Cl	2-furyl	A/B/C/D/-53	2-Br, 4-Cl	2-pyrrolyl
A/B/C/D/-14	2-Br	2-furyl	A/B/C/D/-54	2-Br	2-pyrrolyl
A/B/C/D/-15	2,6-di OH	2-furyl	A/B/C/D/-55	2,6-di OH	2-pyrrolyl
A/B/C/D/-16	2-CH_3	2-furyl	A/B/C/D/-56	2-CH_3	2-pyrrolyl
A/B/C/D/-17	2,4-di Cl	2-furyl	A/B/C/D/-57	2,4-di Cl	2-pyrrolyl
A/B/C/D/-18	3,4-di OCH_3	2-furyl	A/B/C/D/-58	3,4-di OCH_3	2-pyrrolyl
A/B/C/D/-19	2,5-di OCH_3	2-furyl	A/B/C/D/-59	2,5-di OCH_3	2-pyrrolyl
A/B/C/D/-20	3,4,5-tri OCH_3	2-furyl	A/B/C/D/-60	3,4,5-tri OCH_3	2-pyrrolyl
A/B/C/D/-21	4-CH_3	2-thiophenyl	A/B/C/D/-61	4-CH_3	2-pyridinyl
A/B/C/D/-22	4-OCH_3	2-thiophenyl	A/B/C/D/-62	4-OCH_3	2-pyridinyl
A/B/C/D/-23	4-Br	2-thiophenyl	A/B/C/D/-63	4-Br	2-pyridinyl
A/B/C/D/-24	2-OH	2-thiophenyl	A/B/C/D/-64	2-OH	2-pyridinyl
A/B/C/D/-25	3-NO_2	2-thiophenyl	A/B/C/D/-65	3-NO_2	2-pyridinyl
A/B/C/D/-26	4-NO_2	2-thiophenyl	A/B/C/D/-66	4-NO_2	2-pyridinyl
A/B/C/D/-27	4-F	2-thiophenyl	A/B/C/D/-67	4-F	2-pyridinyl
A/B/C/D/-28	4-Cl	2-thiophenyl	A/B/C/D/-68	4-Cl	2-pyridinyl
A/B/C/D/-29	4-OH	2-thiophenyl	A/B/C/D/-69	4-OH	2-pyridinyl
A/B/C/D/-30	2-NH_2	2-thiophenyl	A/B/C/D/-70	2-NH_2	2-pyridinyl
A/B/C/D/-31	3-NH_2	2-thiophenyl	A/B/C/D/-71	3-NH_2	2-pyridinyl
A/B/C/D/-32	2,4-di OH	2-thiophenyl	A/B/C/D/-72	2,4-di OH	2-pyridinyl
A/B/C/D/-33	2-Br, 4-Cl	2-thiophenyl	A/B/C/D/-73	2-Br, 4-Cl	2-pyridinyl
A/B/C/D/-34	2-Br	2-thiophenyl	A/B/C/D/-74	2-Br	2-pyridinyl
A/B/C/D/-35	2,6-di OH	2-thiophenyl	A/B/C/D/-75	2,6-di OH	2-pyridinyl
A/B/C/D/-36	2-CH_3	2-thiophenyl	A/B/C/D/-76	2-CH_3	2-pyridinyl
A/B/C/D/-37	2,4-di Cl	2-thiophenyl	A/B/C/D/-77	2,4-di Cl	2-pyridinyl
A/B/C/D/-38	3,4-di OCH_3	2-thiophenyl	A/B/C/D/-78	3,4-di OCH_3	2-pyridinyl
A/B/C/D/-39	2,5-di OCH_3	2-thiophenyl	A/B/C/D/-79	2,5-di OCH_3	2-pyridinyl
A/B/C/D/-40	3,4,5-tri OCH_3	2-thiophenyl	A/B/C/D/-80	3,4,5-tri OCH_3	2-pyridinyl
A = 80	**B = 80**	**C = 80**	**D = 80**	**Total**	**320**

suggesting favorable oral bioavailability. Additional drug-likeness filters, including Veber's rule, Pan-assay interference compounds (PAINS) alerts, bioavailability scores, and synthetic accessibility indices, were also determined. These parameters collectively provided a multidimensional assessment of the compounds' pharmacokinetic behavior, structural alert liability, and synthetic feasibility, which supports their potential to be good drug candidates.

SwissADME's bioavailability radar gives a quick and easy visual check to see if the compounds have the right properties to be good drugs. The radar involves six key parameters: solubility (log S ≤ 6), saturation (fraction of sp^3-hybridized carbons ≥ 0.25), flexibility (≤9 rotatable bonds), size (molecular weight between 150–500 g/mol), polarity [total polar surface area (TPSA) between 20 and 130 $Å^2$], and lipophilicity (XLOGP3 within −0.7 to +5.0). Compounds that fall inside the pink area are likely to have good bioavailability.

Moreover, blood–brain barrier (BBB) permeability and passive gastrointestinal absorption (human intestinal absorption) were determined using the BOILED-Egg model, which leverages a bidimensional representation based on Wildman and Crippen LogP (WLOGP) (computationally predicted lipophilicity value) and TPSA. According to this model, compounds in the yellow region (yolk) are likely to reach the brain, whereas those in the white region are likely to exhibit efficient passive absorption via the gastrointestinal tract.

2.3. ADMET study

In this study, the pkCSM web tool was utilized to predict the ADMET profiles of the designed compounds. The pkCSM platform utilizes graph-based structural signatures, which encode atomic distance relationships within compounds, to develop and refine robust predictive models. Detailed pharmacokinetic and toxicity parameters were generated for each compound by using this tool. Key descriptors analyzed included intestinal absorption, BBB permeability, central nervous system (CNS) penetration, total renal clearance, hepatotoxicity, hERG-I inhibition (indicative of potential cardiotoxicity), AMES Test (biological assay to assess mutagenicity of compounds), and oral rat acute toxicity (LD_{50}). In addition, physicochemical properties such as TPSA and the number of rotatable bonds were determined to evaluate their influence on drug-likeness and pharmacokinetic performance. The comprehensive *in silico* analysis revealed that most compounds exhibited favorable ADMET characteristics, thereby reinforcing their suitability for further preclinical development.

2.4. Molecular dynamics simulation

Molecular dynamics (MD) simulation is profoundly considered a crucial method for comprehending the dynamic nature of the protein–ligand complex. For each complex, a 100-ns MD simulation production run was performed. The MD simulation was conducted using Gromacs 2021.1, in a Linux operating system environment. In particular, before the simulation production run was initiated, a macromolecular system was prepared. Therefore, ligand structure topology was parameterized using the SwissParam tool, and the protein topology was produced using the CHARMM36 force field. A time step of 2 fs, a constant pressure of 1 atm, and a constant temperature of 300 K were employed throughout the simulation run. Every protein–ligand complex was submerged in a cubic box system, with a minimum distance of 10 Å between the center and the box edge, and the TIP3P water model was used to solve the entire system. Moreover, the entire system was also neutralized by adjusting the required amount of Na^+/Cl^- ions. The steepest descent algorithm was used to minimize all systems to address the overlap and close connections between the atoms. Before the MD simulation production phases, each system was equilibrated with NVT (constant number of Particles, Volume, and Temperature ensemble) followed by NPT (constant number of Particles, Pressure, and Temperature ensemble) for 5 ns each. Finally, a 100-ns run was executed for the MD trajectory, analyzing parameters such as root-mean-square deviation (RMSD) of protein and ligand, root-mean-square fluctuation, and radius of gyration (RoG), which were calculated by using MD simulation. Furthermore, the molecular mechanics generalized born surface area (MM-GBSA) approach was used for binding free energy calculation by MD simulation trajectory using the gmx_MMPBSA package. A total of 2,000 frames from the beginning to the end of the simulation were considered for the estimation of the binding free energy of the selected proposed compound and co-crystal ligand of the VEGFR-2 protein.

3. RESULTS AND DISCUSSION

3.1. Molecular docking analysis

In silico molecular docking method enhances drug discovery efficiency and decreases the cost and time of experiment. Designed compounds were subjected to molecular docking using AutoDock Vina software. The identified protein structure was subjected to quality review and binding site analysis utilizing the PROCHECK and CASTp servers. Almost 90.2% of residues are located in the most preferred regions, depicted in the Ramachandran plot as shown in Figure 2. A single binding pocket was detected in the targeted protein (PDB ID: 4ASD), with an area of 234.669 and a volume of 256.930, as depicted in Figure 3.

3.1.1. Redocking for validation and grid generation

The co-crystallized ligand attached to the protein structure within the binding pocket was removed and subjected to a redocking procedure within the active site. This redocking process gave a binding affinity score of −11.0 kcal/mol and a very small RMSD value of 0.159 Å, meaning the new pose closely matched the original one. This showed that the important interactions with key amino acid residues of the protein were correctly repeated. The redocking pose of the co-crystallized ligand is depicted in Figure 4. A docking grid was established with x-, y-, and z- coordinates of −23.259, 0.347, and −10.064, respectively, ensuring coverage of all key amino acid residues within the active site. The grid box dimensions were set to 40Å × 40Å × 40 Å along the respective axes. The abovementioned dimensions of the grid box were considered while preparing the configuration file for molecular docking.

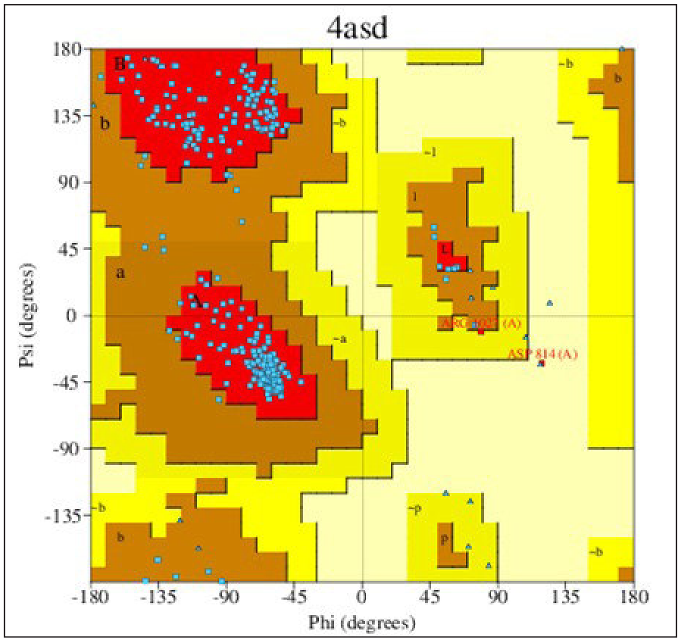

Figure 2. The Ramachandran plot for VEGFR-2 kinase (PDB ID: 4ASD) shows a favored region with 90.2% residues.

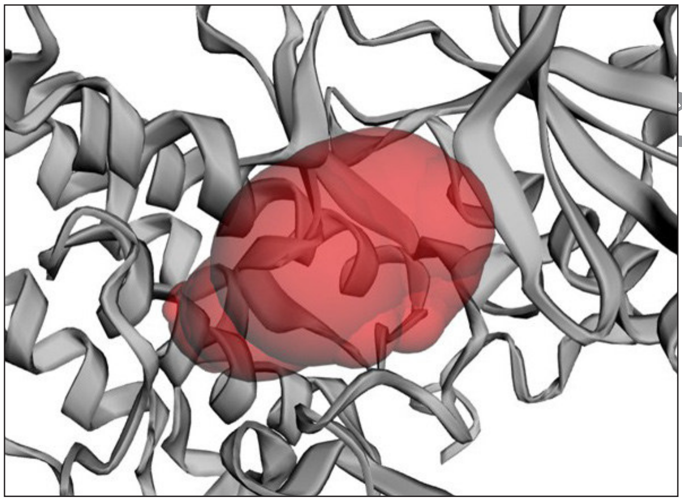

Figure 3. Binding pocket (red) is present in 4 ASD.

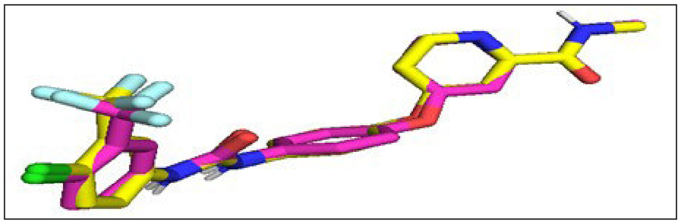

Figure 4. Superimposition of the co-crystallized ligand (pink color) and redocked conformer (yellow color).

Docking simulations were then performed with all relevant information, including binding affinity scores and RMSD values. These parameters were essential for evaluating the strength of ligand–receptor interactions while also providing critical metrics for the precision and reliability of the docking protocol employed.

3.1.2. Post-docking analysis

The resulting docking poses were carefully examined, and those illustrating the most favorable ligand–receptor interactions were selected for further analysis. Among the four designed series comprising a total of 320 compounds, the C series compounds exhibited the highest binding affinities against the target protein. The binding affinities of "C" series compounds ranged from −11.7 to −8.2 kcal/mol. Molecular docking was conducted in three successive rounds, and the top six compounds, all from the C series, consistently maintained strong binding interactions throughout. These six compounds were subsequently shortlisted for further pharmacokinetic and toxicological evaluation. Each selected compound underwent a detailed interaction analysis using the PLIP web server and PyMOL molecular visualization software, and the results were compared with the co-crystallized ligand (sorafenib). The binding affinities and corresponding interaction profiles of these top six compounds and the co-crystallized ligand are summarized in Table 2. The top selected compounds (**C-66, C-46, C-65, C-5, C-64,** and **C-45**) exhibited significant hydrophobic interactions with LEU72, VAL80, ALA98, VAL148, PHE150, LEU217, and PHE229. Consistent hydrogen bonding was observed with ASN155 across all compounds. Additionally, compounds **C-46** and **C-64** demonstrated enhanced binding through supplementary hydrogen bonds with LEU72 and GLY154. π-π stacking interactions with PHE229 were also consistently present in all compounds, contributing to overall binding stability. The co-crystallized ligand exhibited hydrogen bonding interactions with GLU117, GLU117, CYS151, CYS151, and ASP228; hydrophobic interactions with LEU72, VAL80, ALA98, LEU121, VAL131, VAL148, LEU217, ASP228, PHE229, and PHE229; and an additional halogen bond interaction with VAL131. The interactions of the top 6 compounds and the co-crystal ligand at the binding site of the receptor are shown in Figure 5.

3.2. Evaluation of drug-likeness and synthetic accessibility

Numerous studies have demonstrated that the toxicological profiles and adverse effects of anticancer agents are closely correlated with their molecular weight and inherent chemical characteristics. In light of this, we performed a detailed study of pharmacokinetic parameters and important characteristics relevant to the designed derivatives, utilizing the SwissADME web server to determine chemical characteristics and ADME profiles. The results are depicted in Table 3. The selected top 6 compounds and standard drug sorafenib satisfied Lipinski's rule of five; however, only compound **C-64** and sorafenib met the criteria set by Veber's rule. In addition, their predicted oral bioavailability was considered moderate, with an Abbott bioavailability score of 0.55. From a medicinal chemistry viewpoint, the compounds did not trigger alerts for PAINS filters. The synthetic accessibility scores of the top compounds, ranged from 4 to 5, indicating moderate synthetic feasibility. While synthesis may require careful planning, it remains practical

Table 2. Docking Score and interactions between the top 6 compounds and 4ASD.

Compound Code	Binding affinity (kcal/mol)	Hydrophobic interactions	Hydrogen bonding	π-stacking	Halogen bond
C-66	−11.7	LEU72, VAL80, VAL80, ALA98, VAL148, PHE150, LEU217, PHE229, PHE229	ASN155	PHE229	-
C-46	−11.2	LEU72, VAL80, VAL80, ALA98, VAL148, PHE150, LEU217, PHE229	LEU72, ASN155	PHE229	-
C-65	−11	LEU72, VAL80, VAL80, ALA98, VAL148, PHE150, PHE150, LEU217, PHE229	ASN155	PHE229	-
C-5	−10.8	LEU72, VAL80, VAL80, ALA98, VAL148, PHE150, PHE150, LEU217, PHE229	ASN155	PHE229	-
C-64	−10.6	LEU72, LEU72, VAL80, VAL131, VAL131, VAL148, PHE150, LEU217, PHE229	GLY154, ASN155	PHE229	-
C-45	−10.6	LEU72, VAL80, VAL80, ALA98, VAL148, PHE150, LEU217, PHE229	ASN155	PHE229	-
Co-crystal ligand (Sorafenib)	−11.7	LEU72, VAL80, ALA98, LEU121, VAL131, VAL148, LEU217, ASP228, PHE229, PHE229	GLU117, GLU117, CYS151, CYS151, ASP228	-	VAL131

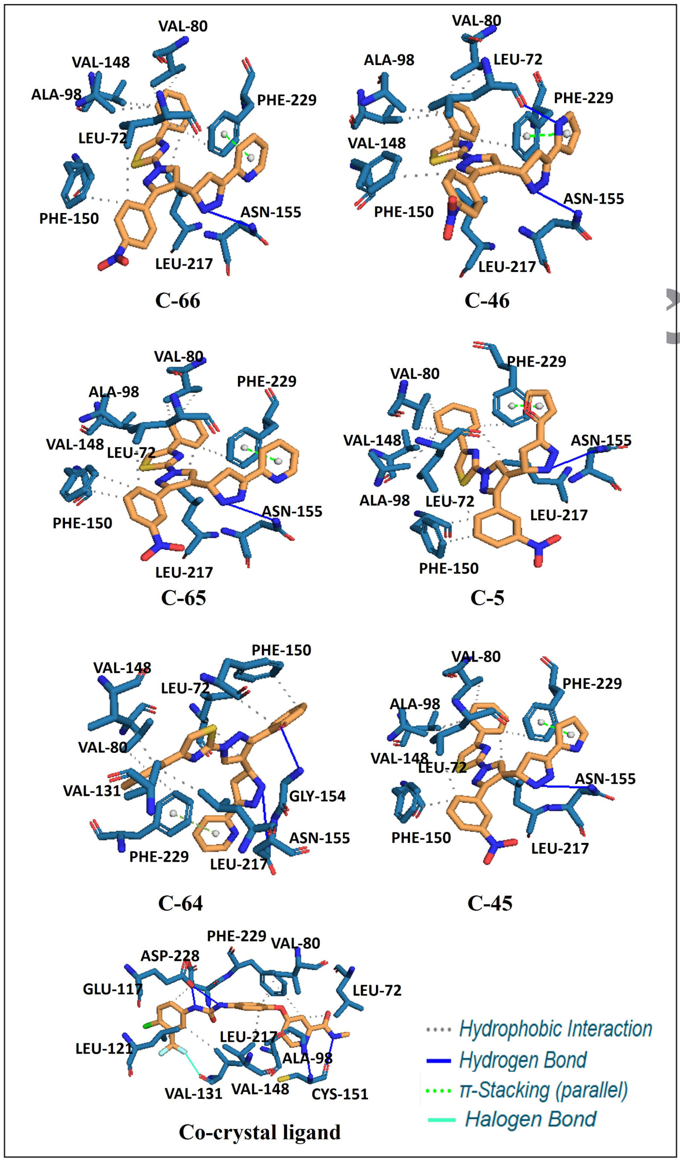

Figure 5. The interactions of top 6 compounds and the co-crystal ligand with amino acids.

and acceptable for early-stage drug development. Overall, the compounds demonstrated favorable druggability, meeting Lipinski's rule of five, showing promising oral absorptivity, and demonstrating synthetic accessibility. These factors demonstrate their potential as chemotherapeutic agents or drug leads.

3.3. ADMET prediction

The ADMET profiles of the designed compounds were comprehensively evaluated to determine their viability as prospective therapeutic agents, with the corresponding data compiled in Table 4. All compounds demonstrated high predicted gastrointestinal absorption, indicative of efficient oral uptake, while concurrently exhibiting limited potential for CNS distribution. In the context of BBB permeability, a Log PS (permeability-surface area product) value exceeding −2 is generally indicative of significant CNS penetration, whereas values below −3 are associated with an inability to traverse the BBB. All compounds fall within an intermediate range (−2.099 to −1.961), indicating a reduced likelihood of CNS exposure. The propensity for metabolic interactions and toxicity was further interrogated through *in silico* predictions of cytochrome P450 (CYP) isoenzyme inhibition. As CYP enzymes are implicated in the biotransformation of approximately 50% of clinically used drugs, their inhibition can lead to adverse drug–drug interactions and altered pharmacokinetics. All the compounds are CYP3A4 substrates and inhibit CYP3A4, CYP2C19, and CYP2C9, indicating a potential for drug–drug interactions. However, this metabolic profile aligns with sorafenib, a clinically approved VEGFR-2 inhibitor, suggesting that the interaction risk is acceptable and manageable in the drug development context. Nevertheless, the observed CYP450 inhibition highlights the need for further investigation during later development stages to assess and mitigate potential drug–drug interaction risks. All top compounds exhibited renal clearance values ranging from 0.399 to 0.656, indicative of extended systemic retention and potential for sustained therapeutic effect. Notably, among the top six candidates, compound C-64 showed the lowest predicted total renal clearance (0.399). Toxicological evaluations were subsequently carried out across four critical endpoints: mutagenicity, hepatotoxicity, cardiotoxicity, and

Table 3. Drug-likeness and synthetic accessibility assessment of selected compounds.

Compounds	C-66	C-46	C-65	C-5	C-64	C-45	Co-crystal ligand (sorafenib)
Molecular weight	493.54	481.53	493.54	482.51	464.54	481.53	464.82
Hydrogen bond donors	1	2	1	1	2	2	3
Hydrogen bond acceptors	6	5	6	6	5	5	7
LogP	3.22	3.04	3.22	3.04	2.75	3.04	2.91
TPSA	142.05	144.95	142.05	142.30	116.46	144.95	92.35
Rotatable bonds	6	4	6	6	5	6	9
Lipinski's rule of five violations	0	0	0	0	0	0	0
Veber's rule violations	1*	1*	1*	1*	0	1*	0
Synthetic accessibility	4.48	4.46	4.51	4.50	4.46	4.49	2.87
Bioavailability score	0.55	0.55	0.55	0.55	0.55	0.55	0.55

*TPSA > 140.

Table 4. Predicted ADMET parameters of selected compounds

	Compounds		C-66	C-46	C-65	C-5	C-64	C-45	Co-crystal ligand (sorafenib)
Absorption	Human intestinal absorption		100	100	100	100	94.546	100	88.528
Distribution	LogBB		−1.264	−1.115	−1.194	−1.143	−0.994	−1.047	−1.449
	LogPS		−2.074	−2.052	−2.099	−1.961	−2.083	−2.056	−1.878
Metabolism	Substrate	CYP2D6	No	No	No	No	No	No	No
		CYP3A4	Yes	Yes	Yes	Yes	Yes	Yes	Yes
	Inhibitors	CYP11A2	No	No	No	No	No	No	No
		CYP2C19	Yes	Yes	Yes	Yes	Yes	Yes	Yes
		CYP2C9	Yes	Yes	Yes	Yes	Yes	Yes	Yes
		CYP2D6	No	No	No	No	No	No	No
		CYP3A4	Yes	Yes	Yes	Yes	Yes	Yes	Yes
Excretion	Total renal clearance		0.484	0.536	0.605	0.57	0.399	0.656	−0.214
Toxicity	Hepatotoxicity		Yes	Yes	Yes	No	No	No	Yes
	hERG-I inhibitor		No	No	No	No	No	No	No
	AMES toxicity		Yes	Yes	Yes	Yes	No	Yes	No
	Oral rat acute toxicity (LD_{50})		2.887	2.887	2.861	2.892	3.106	2.892	3.155

oral acute toxicity (LD_{50}). As detailed in Table 4, compounds **C-5, C-45**, and **C-64** were predicted to be non-hepatotoxic, whereas **C-66, C-46, C-65,** and sorafenib were found to be hepatotoxic. While none of the tested compounds showed cardiotoxic potential, mutagenicity was observed in **C-66, C-46, C-65, C-5**, and **C-45**. Notably, while Sorafenib, the standard reference compound, was identified as hepatotoxic, compound **C-64** was free from all evaluated forms of toxicity, including hepatotoxicity, cardiotoxicity, and mutagenicity. Furthermore, **C-64** demonstrated a high LD_{50} value, indicative of low acute oral toxicity and a broad safety margin. These attributes collectively highlight **C-64** as the most promising candidate, with an excellent overall ADMET profile, reinforcing its potential as a lead compound for further development.

In addition to the core pharmacokinetic and safety advantages, compound **C-64** was further assessed using advanced drug-likeness metrics provided by SwissADME. The bioavailability radar (Fig. 6) confirmed that **C-64** aligns well with the optimal physicochemical space for oral drug candidates in terms of lipophilicity, molecular size, polarity, solubility, and flexibility; however, a deviation in the saturation parameter was noted, reflecting a reduced fraction of sp^3-hybridized carbons compared to the ideal threshold.

Furthermore, the compound was evaluated using the BOILED-Egg model (Fig. 6), where it was located within the white region of the WLOGP versus TPSA plot. This region is associated with a high probability of passive gastrointestinal absorption, suggesting effective oral uptake. Such a positioning reflects a well-balanced lipophilic–polar profile, a crucial factor in membrane permeability, and reinforces the compound's suitability for oral administration and systemic bioavailability.

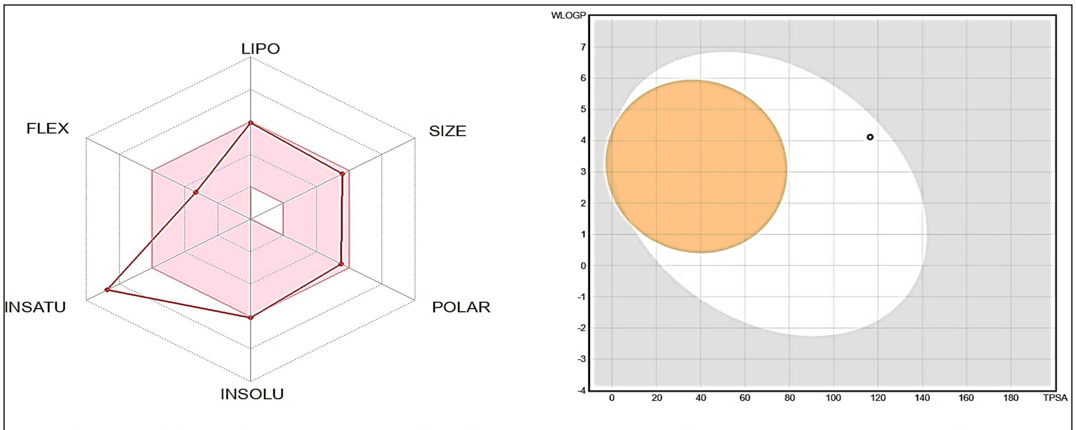

Bioavailability Radar representations of C-64 **Boiled Egg representations of C-64**

Figure 6. Boiled-Egg representations with bioavailability radar images of the compound C-64 showing their physicochemical behavior.

3.4. MD simulation

MD simulation is a powerful computational technique extensively used to explore the dynamic and structural properties of protein–ligand complexes. Due to its excellent safety profile, lacking hepatotoxicity, cardiotoxicity, and mutagenicity, compound **C-64** was selected for in-depth investigation using MD simulation. A 100-ns simulation was conducted to evaluate the stability and interaction dynamics of the C-64–VEGFR-2 complex. For comparative purposes, the co-crystallized ligand of VEGFR-2 was subjected to identical simulation conditions. This strategy allowed for a thorough comparison of the dynamic behavior of C-64 with the standard ligand, reinforcing its potential as a safe and effective lead compound. Key parameters, such as RMSD, RMSF, intermolecular hydrogen bonds, RoG, free energy landscape (FEL), solvent accessible surface area (SASA), principal component analysis (PCA), and dynamical cross-correlated matrix or maps (DCCM), were extracted from the simulation trajectories. Furthermore, the entire simulation trajectory was utilized to estimate the binding free energy of each complex using the MM-GBSA method.

3.4.1. RMSD profile analysis

To assess the conformational and binding stability of the protein–ligand complexes, the RMSD of the protein backbone was calculated from the MD simulation trajectory. Higher backbone RMSD typically reflects conformational rearrangements, whereas lower values suggest greater structural stability. A stable RMSD profile with minimal fluctuations indicates system equilibration. In this study, the VEGFR-2 backbone RMSD for complexes with C-64 and the co-crystallized ligand was calculated and is shown in Figure 7. The average RMSD values were 0.246 nm for C-64 and 0.188 nm for the co-crystal ligand, with both systems displaying consistent trajectories. Although the C-64 complex exhibited a slightly higher deviation, overall stability was maintained.

Ligand RMSD was also analyzed to evaluate the positional stability of the ligands during the simulation (Fig. 8). The difference between maximum and minimum RMSD was 0.226 nm for C-64 and 0.120 nm for the co-crystal ligand, indicating limited deviation from their initial binding poses. These findings indicate that both ligands maintained stable binding within the VEGFR-2 active site throughout the simulation.

3.4.2. Root-mean-square fluctuation

The RMSF, a key parameter for assessing the flexibility of individual amino acid residues, was systematically calculated for both complexes. These analyses offer valuable insight into the residue-level dynamics of VEGFR-2. Notably, while the catalytic region remained stable, certain residues exhibited higher fluctuations, reflecting the balance between structural rigidity and flexibility in the presence of C-64 (Fig. 9).

Moreover, the combined evaluation of protein backbone RMSD, ligand RMSD, and RMSF underscores a key finding: compound C-64 exhibited no significant conformational changes throughout the simulation. This observation highlights the structural stability and robustness of C-64 within the VEGFR-2 binding site.

3.4.2. Radius of gyration

RoG is another key parameter derived from MD simulation trajectories, used to evaluate the compactness and structural rigidity of the protein–ligand complex over time. The RoG values for the VEGFR-2 complexes with C-64 and the co-crystallized ligand were calculated and are presented in Figure 10. The difference between the maximum and minimum RoG values provides insight into the flexibility and compactness of the system during the simulation. This difference was found to be 0.125 nm for C-64 and 0.090 nm for the co-crystal ligand. Notably, VEGFR-2 bound to C-64 exhibited RoG variations similar to those of the co-crystal ligand between 40 and 100 ns of the simulation. Overall, the relatively stable RoG profiles across both complexes suggest that the structural compactness of the system was maintained throughout the simulation period.

3.4.3. Intermolecular H-bond interactions

Intermolecular hydrogen bonds between the protein and ligand play a vital role in stabilizing the ligand within the

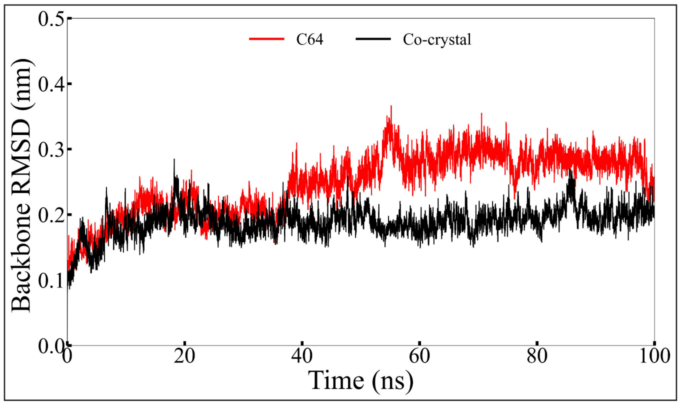

Figure 7. Backbone RMSD of the compound C-64 and the co-crystallized ligand.

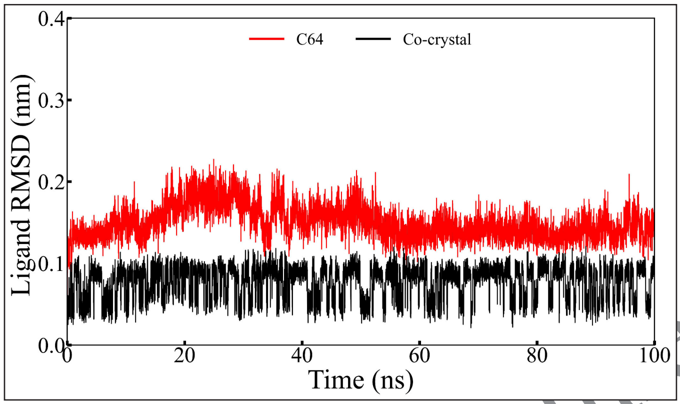

Figure 8. Ligand RMSD of the compound C-64 and the co-crystallized ligand.

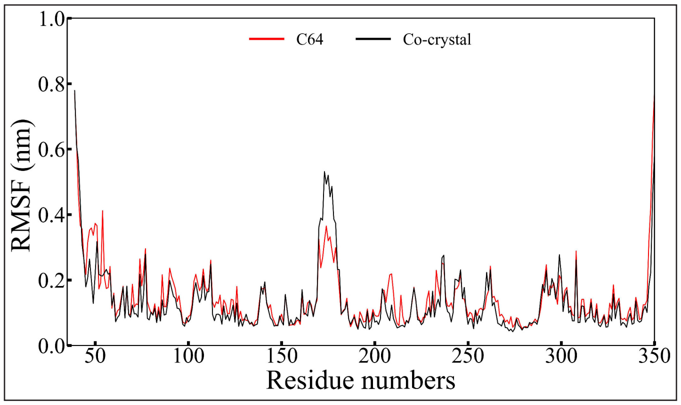

Figure 9. RMSF of VEGFR-2 bound with C-64 and the co-crystallized ligand.

active site during MD simulations. The number of hydrogen bonds formed in each simulation system was calculated and is illustrated in Figure 11. In the majority of simulation frames for both complexes, at least one hydrogen bond was maintained. In frames where hydrogen bonds were absent, the ligand remained bound through other non-hydrogen bonding interactions. Notably, both C-64 and the co-crystallized ligand formed up to six hydrogen bonds at certain points during the simulation, indicating strong and transient interactions contributing to binding stability.

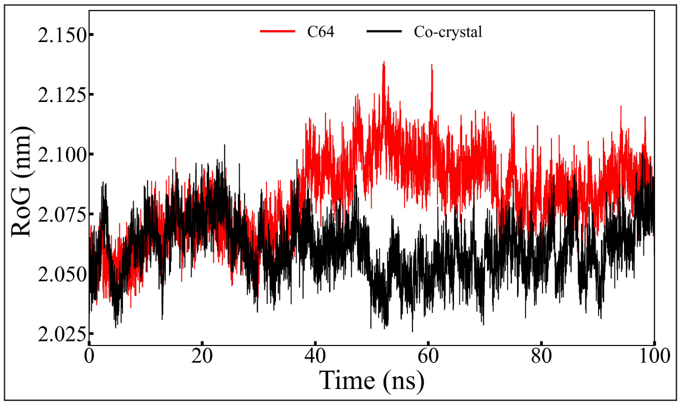

Figure 10. The radius of gyration of VEGFR-2 is bound with C-64 and the co-crystal ligand.

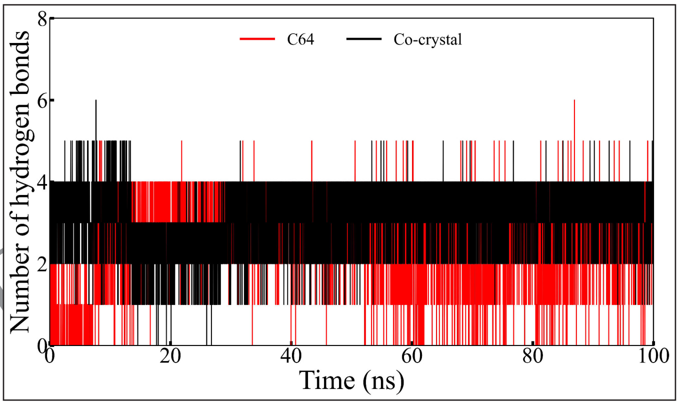

Figure 11. Number of hydrogen bonds formed between VEGFR-2 and compounds.

3.4.4. Free energy landscape

The FEL of the VEGFR-2 protein was analyzed to evaluate the conformational stability of the protein–ligand complexes, with the results presented in Figure 12. The FEL approach provides insight into the thermodynamic stability of the system by mapping the conformational space sampled during the MD simulation. A greater number of deep and scattered energy minima typically reflects frequent conformational changes and indicates structural instability or difficulty in achieving a stable native state. In contrast, both the C-64 and co-crystallized ligand complexes exhibited relatively flat and well-defined energy minima on the FEL plot. This suggests that both systems experienced fewer large-scale conformational shifts and maintained stable, low-energy conformations throughout the simulation. The flatness and uniformity of the minima for C-64, comparable to that of the standard ligand, indicate that C-64 forms a thermodynamically stable complex with VEGFR-2, further supporting its potential as a reliable and stable lead compound.

3.4.5. Solvent accessible surface area

SASA measures the surface area of a protein that is accessible to solvent molecules, providing insights into protein folding and stability. SASA analysis revealed that both VEGFR-2 complexes bound with C-64, and the co-crystallized ligand exhibited values ranging from 160 to 185 nm^2, with

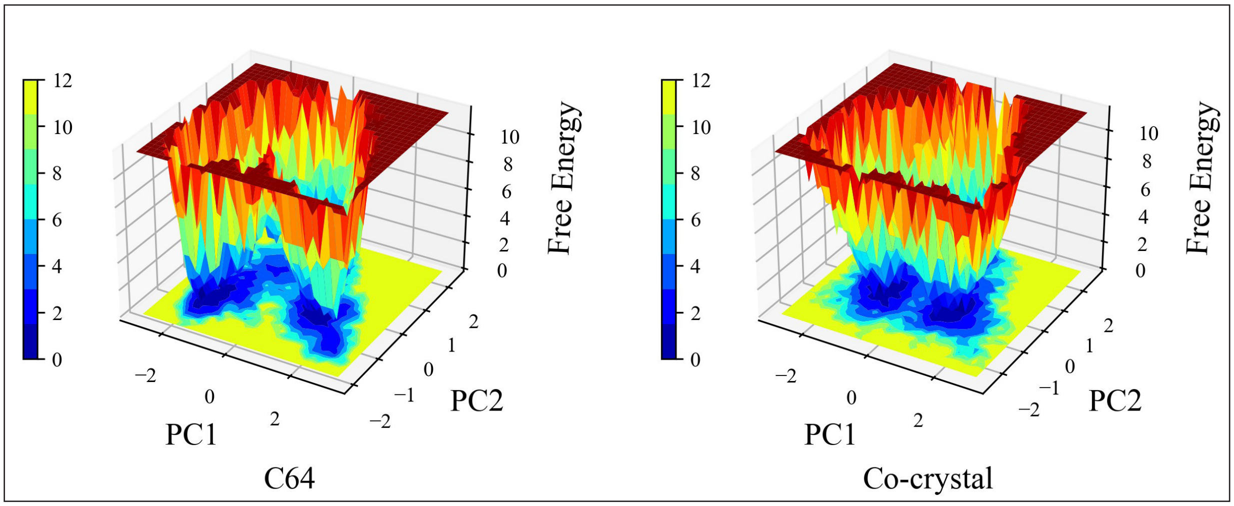

Figure 12. Free energy landscape graphs of C-64 and the co-crystal ligand.

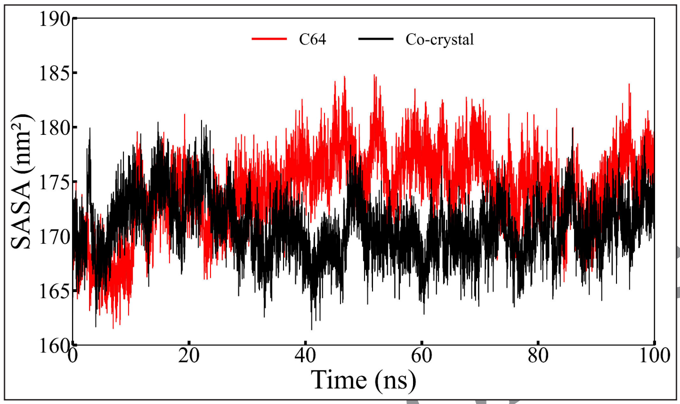

Figure 13. SASA.

similar fluctuation patterns observed throughout the 100 ns MD simulation. Both systems showed elevated SASA values during the 30–80 ns interval. Overall, the consistent or gradually decreasing SASA values over time suggest a tendency toward protein folding and structural stabilization. As illustrated in Figure 13, the SASA profiles remained largely steady during the simulation, indicating that the binding of C-64 or the co-crystal ligand did not induce dissociation or significant destabilization of the VEGFR-2 protein in its dynamic state.

3.4.6. Principal component analysis

PCA was performed to identify the dominant motions within the protein–ligand complexes during the MD simulation (Fig. 14). The first three principal components (PCA 1, 2, and 3) represent the largest conformational variances in the system. PCA effectively highlights critical atomic movements and overall flexibility, offering insights into dynamic behavior that can inform inhibitor design. The PCA plots show distinct clustering patterns for each complex. The co-crystallized ligand formed tight, compact clusters, indicating lower molecular flexibility. In contrast, C-64 exhibited more dispersed clusters, suggesting higher flexibility throughout the simulation. This increased flexibility of the C-64 complex may contribute to enhanced inhibitory potential, supporting its promise as a VEGFR-2 inhibitor.

3.4.7. Dynamical cross-correlated matrix or maps

DCCMs were used to analyze residue motion correlations in VEGFR-2 bound to compound C-64 and the co-crystallized ligand during MD simulation (Fig. 15). DCCM reveals coordinated atomic movements, ranging from −1 (anticorrelated) to 1 (correlated). From Figure 15, it has been observed that yellow shades indicate strong positive correlations (atoms move together), blue shades indicate negative correlations (atoms move oppositely), and deep green represents little correlation (independent motion). The VEGFR-2–C-64 complex displays more extensive yellow areas than the co-crystal ligand, indicating greater coordinated motions. This suggests that C-64 binding promotes more synchronized protein dynamics, potentially impacting VEGFR-2 function and ligand interaction.

3.4.8. Calculation of the binding free energy through MM-GBSA approach

MM-GBSA is a reliable method for estimating binding affinities from MD simulation trajectories. Binding free energies for compound C-64 and the co-crystallized ligand were calculated using 2,000 simulation frames, with detailed energy contributions and values summarized in Table 5. The results revealed MM-GBSA binding energies (ΔG_{bind}) of −45.54 (±3.31) kcal/mol for C-64 and −48.27 (±2.56) kcal/mol for the co-crystal ligand. The full binding free energy profile over the simulation is shown in Figure 16. Compound C-64 demonstrated binding free energies comparable to the co-crystallized ligand, likely reflecting similar interactions with key VEGFR-2 residues. These results underscore the promising potential of C-64 as an effective VEGFR-2 inhibitor.

3.5. Summary

In this study, a series of pyrazole–pyrazoline derivatives bearing diverse heterocyclic substitutions was designed with the aim to enhance VEGFR-2 inhibitory activity. Among the

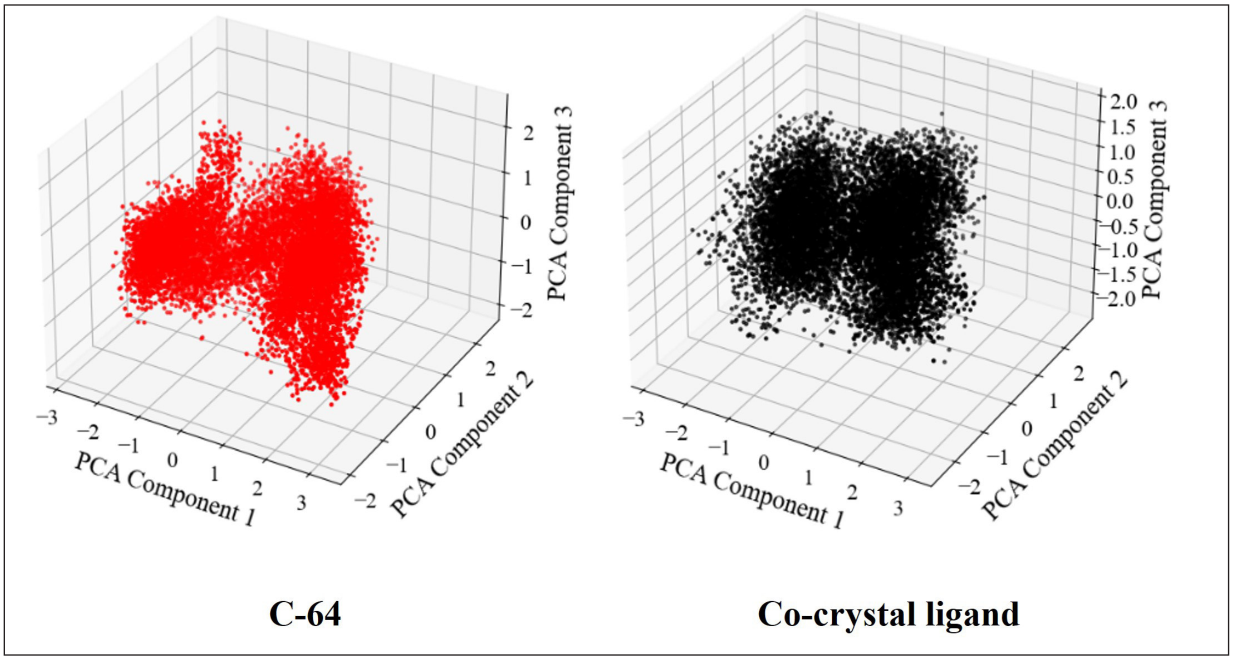

C-64

Co-crystal ligand

Figure 14. The PCA of C-64 and the co-crystal ligand.

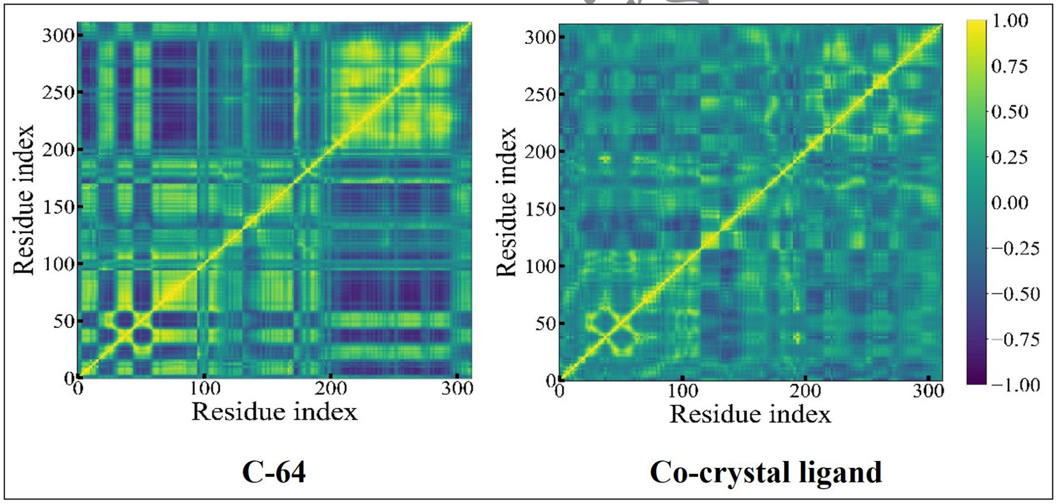

C-64

Co-crystal ligand

Figure 15. DCCM plot representing correlation in the residue motions for MD simulations for VEGFR-2 protein backbone bound with C-64 and co-crystal ligand.

Table 5. MM-GBSA energies of C-64 along with the co-crystal ligand.

Compounds	ΔG_{bind}	ΔE_{VDW}	ΔE_{ELE}	SD (±)
C-64	−45.54	−46.28	−23.36	3.31
Co-crystal ligand	−48.27	−57.48	−32.79	2.56

four designed series, the C-series, characterized by a 4-phenyl-thiazol-2-yl substitution at the 1-position of the pyrazole ring, demonstrated superior binding affinity toward VEGFR-2. Approximately 15 compounds from this series exhibited high docking scores (ranging from −11.7 to −10.3), surpassing those of other series (scores below −10.3). The top six candidates from the C-series were selected for further evaluation of their pharmacokinetic, physicochemical, and toxicological properties, and their profiles were compared against sorafenib. Among these, compound **C-64** emerged as the most promising candidate, showing full compliance with Lipinski's rule of five and Veber's rule, indicative of favorable oral bioavailability and drug-likeness comparable to Sorafenib. Advanced ADMET analysis revealed that **C-64** was devoid of predicted toxicological risks, including hepatotoxicity, mutagenicity (AMES test), cardiotoxicity (hERG-I inhibition), and acute oral toxicity. In contrast, sorafenib was predicted to be hepatotoxic. **C-64** exhibited the highest LD_{50} among the top candidates, indicating a broad safety margin and low acute toxicity. Its low predicted clearance rate suggests

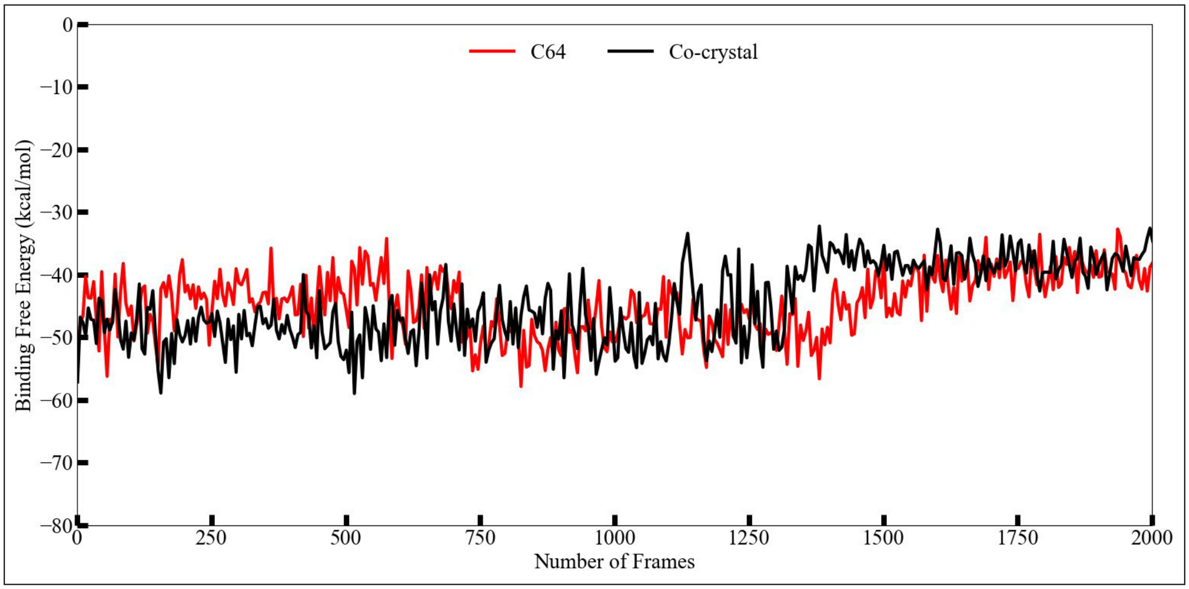

Figure 16. Binding free energy of C-64 and co-crystal ligand toward VEGFR-2.

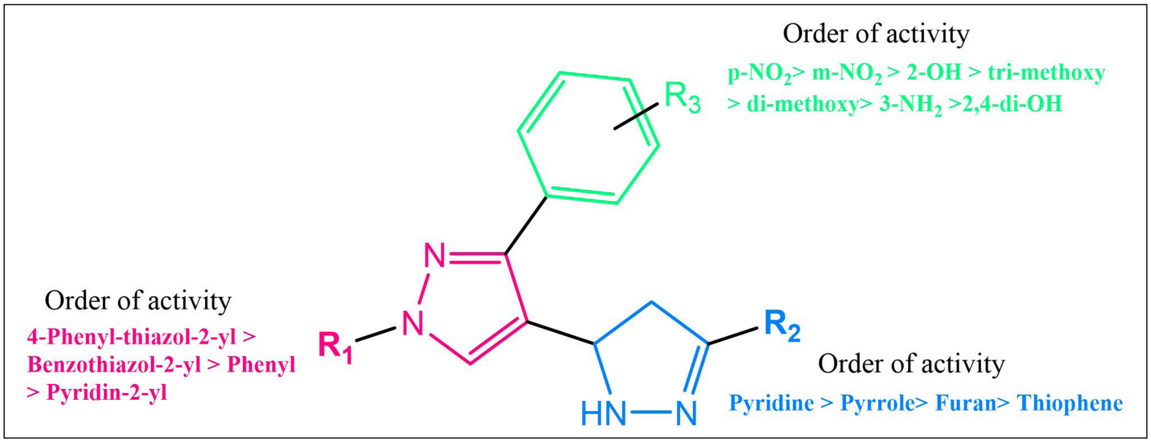

Figure 17. SAR of pyrazole–pyrazoline derivatives.

prolonged systemic retention and sustained therapeutic potential. Bioavailability radar and BOILED-Egg analysis confirmed good oral absorption and gastrointestinal permeability, with only minor structural optimization needed. Notably, the MD simulation results for compound **C-64** closely mirrored those of sorafenib, in terms of stability and dynamic behavior within the binding pocket. Additionally, **C-64** showed a synthetic accessibility score of 4.48, reflecting moderate synthetic complexity that is well within acceptable limits for drug development. Collectively, these findings highlight C-64 as a safe, bioavailable, and synthetically feasible lead candidate for VEGFR-2-targeted anticancer therapy.

3.6. SAR of pyrazole-pyrazoline derivatives

- Among the four series, 4-phenyl-thiazol-2-yl substitution at the first position of the pyrazole ring possessed the highest binding affinity.
- The compounds bearing a nitro group at the *para* or *meta* position or a hydroxy group at the *ortho* position of the phenyl ring at the third position of the pyrazole, exhibited the highest affinity.
- Pyridine substitution on the pyrazoline moiety demonstrated higher binding affinity compared to pyrrole, furan, or thiophene substitutions.
- Among the top six screened compounds, compound **C-64** featuring an *ortho* hydroxy group on the phenyl ring and a pyridine moiety attached to the pyrazoline scaffold emerged as the most promising lead candidate, as evidenced by its favorable pharmacokinetic, physicochemical, and toxicological properties along with optimum binding affinity, when compared to standard sorafenib(The SAR observations are summarized in Fig. 17)

4. CONCLUSION

In this study, a series of pyrazole–pyrazoline derivatives substituted with various heterocyclic moieties were rationally designed and evaluated through an *in silico* approach targeting VEGFR-2, a key regulator of angiogenesis. Molecular docking studies demonstrated that several compounds exhibited strong binding affinities and favorable interactions with critical active site residues of the VEGFR-2 kinase. Subsequent evaluation of drug-likeness parameters using the SwissADME platform, alongside ADMET profiling via the pkCSM web server, confirmed that the selected compounds demonstrated favorable pharmacokinetic properties, low predicted toxicity, and overall compliance with essential drug-likeness rules. Among the tested series, compound C-64 emerged as the most promising lead candidate, exhibiting an optimal combination of high binding affinity, compliance with both Lipinski's rule of five and Veber's rule, and absence of predicted hepatotoxicity, cardiotoxicity, and mutagenicity. It also demonstrated a high LD_{50} value, suggesting a wide safety margin, and the lowest predicted clearance, indicating prolonged systemic retention. Furthermore, despite a minor deviation in the saturation parameter, C-64 aligned well with key physicochemical parameters in the bioavailability radar and was located in the white region of the BOILED-Egg model, signifying a high probability of efficient passive gastrointestinal absorption. Collectively, these results highlight compound C-64 as a compelling VEGFR-2-targeted anti-angiogenic scaffold with significant potential for further optimization and preclinical development in the context of cancer therapeutics. Moreover, we acknowledge that the current study is limited to computational analyses. While these results provide valuable preliminary insights, we recommend further experimental validation of compound **C-64** through *in vitro* or *in vivo* assays, such as kinase inhibition or cytotoxicity studies, to confirm its biological efficacy.

5. ACKNOWLEDGEMENTS

The authors are grateful to the Mahatma Jyotiba Phule Research and Training Institute (MAHAJYOTI), Maharashtra State, for awarding the Mahatma Jyotiba Phule Research Fellowship-2022 dated 13/12/2022 [MAHAJYOTI/2022/Ph.D.Fellow/1002(246)].

6. AUTHOR CONTRIBUTIONS

All authors made substantial contributions to conception and design, acquisition of data, or analysis and interpretation of data; took part in drafting the article or revising it critically for important intellectual content; agreed to submit to the current journal; gave final approval of the version to be published; and agree to be accountable for all aspects of the work. All the authors are eligible to be an author as per the International Committee of Medical Journal Editors (ICMJE) requirements/guidelines.

7. CONFLICTS OF INTEREST

The authors report no financial or any other conflicts of interest in this work.

8. ETHICAL APPROVALS

This study does not involve experiments on animals or human subjects.

9. DATA AVAILABILITY

All the data is available with the authors and shall be provided upon request.

10. PUBLISHER'S NOTE

All claims expressed in this article are solely those of the authors and do not necessarily represent those of the publisher, the editors and the reviewers. This journal remains neutral with regard to jurisdictional claims in published institutional affiliation.

11. USE OF ARTIFICIAL INTELLIGENCE (AI)-ASSISTED TECHNOLOGY

The authors declares that they have not used artificial intelligence (AI)-tools for writing and editing of the manuscript, and no images were manipulated using AI.

REFERENCES

1. Reddy VG, Reddy TS, Jadala C, Reddy MS, Sultana F, Akunuri R, *et al*. Pyrazolo-benzothiazole hybrids: synthesis, anticancer properties and evaluation of antiangiogenic activity using in vitro VEGFR-2 kinase and *in vivo* transgenic zebrafish model. Eur J Med Chem. 2019;15:182. doi: https://doi.org/10.1016/j.ejmech.2019.111609
2. Ahmed MF, Santali EY, El-Haggar R. Novel piperazine–chalcone hybrids and related pyrazoline analogues targeting VEGFR-2 kinase; design, synthesis, molecular docking studies, and anticancer evaluation. J Enzyme Inhib Med Chem. 2021;36(1):307–18. doi: https://doi.org/10.1080/14756366.2020.1861606
3. Ravula P, Vamaraju HB, Paturi M, Sharath Chandra JNGN. Design, synthesis, *in silico* and antiproliferative evaluation of novel pyrazole derivatives as VEGFR-2 inhibitors. Arch Pharm (Weinheim). 2018;351(1):e1700234. doi: https://doi.org/10.1002/ardp.201700234
4. Ding Y, Liu K, Zhao X, Lv Y, Yu R, Kang C. Design, synthesis, and antitumor activity of novel benzoheterocycle derivatives as inhibitors of vascular endothelial growth factor receptor-2 tyrosine kinase. J Chem Res. 2020;44(5–6):286–94. doi: https://doi.org/10.1177/1747519819899067
5. Mohamed TK, Batran RZ, Elseginy SA, Ali MM, Mahmoud AE. Synthesis, anticancer effect and molecular modeling of new thiazolylpyrazolyl coumarin derivatives targeting VEGFR-2 kinase and inducing cell cycle arrest and apoptosis. Bioorg Chem. 2019;85:253–73. doi: https://doi.org/10.1016/j.bioorg.2018.12.040
6. El-Helby AGA, Sakr H, Eissa IH, Al-Karmalawy AA, El-Adl K. Benzoxazole/benzothiazole-derived VEGFR-2 inhibitors: design, synthesis, molecular docking, and anticancer evaluations. Arch Pharm (Weinheim). 2019;352(12):e1900178. doi: https://doi.org/10.1002/ardp.201900178
7. Wang XR, Wang S, Li WB, Xu KY, Qiao XP, Jing XL, *et al*. Design, synthesis and biological evaluation of novel 2-(4-(1H-indazol-6-yl)-1H-pyrazol-1-yl)acetamide derivatives as potent VEGFR-2 inhibitors. Eur J Med Chem. 2021;213:113192. doi: https://doi.org/10.1016/j.ejmech.2021.113192
8. Thaher BA, Arnsmann M, Totzke F, Ehlert JE, Kubbutat MHG, Schächtele C, *et al*. Tri- and tetrasubstituted pyrazole derivates: regioisomerism switches activity from p38MAP kinase to important cancer kinases. J Med Chem. 2012;55(2):961–5. doi: http://dx.doi.org/10.1021/jm201391u
9. Adams CM, Anderson K, Artman G, Bizec JC, Cepeda R, Elliott J, *et al*. The Discovery of N-(1-Methyl-5-(trifluoromethyl)-1H-pyrazol-3-yl)-5-((6- ((methylamino) methyl) pyrimidin-4-yl)oxy)-1H-indole-1-carboxamide (Acrizanib), a VEGFR-2 inhibitor specifically designed for topical ocular delivery, as a therapy for neovascular age-related macular degeneration. J Med Chem. 2018;61(4):1622–35.. doi: https://doi.org/10.1021/acs.jmedchem.7b01731
10. Ruzi Z, Bozorov K, Nie L, Zhao J, Aisa HA. Novel pyrazolo[3,4-d] pyrimidines as potential anticancer agents: synthesis, VEGFR-2 inhibition, and mechanisms of action. Biomed Pharmacother. 2022;156:113948. doi: https://doi.org/10.1016/j.biopha.2022.113948

11. Alam R, Alam A, Panda AK, Rahisuddin. Design, synthesis and cytotoxicity evaluation of pyrazolyl pyrazoline and pyrazolyl aminopyrimidine derivatives as potential anticancer agents. Med Chem Res. 2018;27(2):560–70. doi: http://dx.doi.org/10.1515/hc-2016-0042
12. Srinivasa Reddy T, Kulhari H, Ganga Reddy V, Subba Rao AV, Bansal V, Kamal A, *et al*. Synthesis and biological evaluation of pyrazolo-triazole hybrids as cytotoxic and apoptosis inducing agents. Org Biomol Chem. 2015;13(40):10136–49. doi: https://doi.org/10.1039/C9OB90120E
13. Alam R, Wahi D, Singh R, Sinha D, Tandon V, Grover A, *et al*. Design, synthesis, cytotoxicity, HuTopoIIα inhibitory activity and molecular docking studies of pyrazole derivatives as potential anticancer agents. Bioorg Chem. 2016;69:77–90. doi: https://doi.org/10.1016/j.bioorg.2016.10.001
14. Dawood DH, Nossier ES, Ali MM, Mahmoud AE. Synthesis and molecular docking study of new pyrazole derivatives as potent anti-breast cancer agents targeting VEGFR-2 kinase. Bioorg Chem. 2020;101:103916. doi: https://doi.org/10.1016/j.bioorg.2020.103916
15. Ashour GRS, Qarah AF, Alrefaei AF, Alalawy AI, Alsoliemy A, Alqahtani AM, *et al*. Synthesis, modeling, and biological studies of new thiazole-pyrazole analogues as anticancer agents. J Saudi Chem Soc. 2023;27(4):101669. doi: https://doi.org/10.1016/j.jscs.2023.101669
16. Upadhyay N, Tilekar K, Safuan S, Kumar AP, Schweipert M, Meyer-Almes FJ, *et al*. Multi-target weapons: diaryl-pyrazoline thiazolidinediones simultaneously targeting VEGFR-2 and HDAC cancer hallmarks. RSC Med Chem. 2021;12(9):1540–54. doi: https://doi.org/10.1039/D1MD00125F
17. Wang M, Xu S, Lei H, Wang C, Xiao Z, Jia S, *et al*. Design, synthesis and antitumor activity of Novel Sorafenib derivatives bearing pyrazole scaffold. Bioorg Med Chem. 2017;25(20):5754–63. doi: https://doi.org/10.1016/j.bmc.2017.09.003
18. Wickens P, Kluender H, Dixon J, Brennan C, Achebe F, Bacchiocchi A, *et al*. SAR of a novel “Anthranilamide Like” series of VEGFR-2, multi protein kinase inhibitors for the treatment of cancer. Bioorg Med Chem Lett. 2007;17(15):4378–81. doi: http://dx.doi.org/10.1016/j.bmcl.2007.02.075
19. Eldebss TMA, Gomha SM, Abdulla MM, Arafa RK. Novel pyrrole derivatives as selective CHK1 inhibitors: design, regioselective synthesis and molecular modeling. Med Chem Comm. 2015;6(5):852–9. doi: https://doi.org/10.1039/C4MD00560K
20. Underiner TL, Ruggeri B, Aimone L, Albom M, Angeles T, Chang H, *et al*. TIE-2/VEGF-R2 SAR and *in vitro* activity of C3-acyl dihydroindazolo[5,4-a]pyrrolo[3,4-c]carbazole analogs. Bioorg Med Chem Lett. 2008;18:2368–2372. doi: https://doi.org/10.1016/j.bmcl.2008.02.069

How to cite this article:
Wanode DM, Bhendarkar KP, Khedekar PB. Discovery of pyrazole-pyrazoline derivatives as VEGFR-2 kinase inhibitors: *In-silico* approach. J Appl Pharm Sci. 2025. Article in Press.
http://doi.org/10.7324/JAPS.2026.256031